Dynamic Propeller Noise Reduction using Synchrophasing Control based on an Extremum-Seeking Algorithm

Adrián Parra Lafuente* Rudy Cepeda-Gomez[‡]; Andres Lopez Pulzovan, Thomas F. Geyer§

2025

Institute of Electrified Aero Engines, German Aerospace Center (DLR), Lieberoser Straße 13a, 03046 Cottbus, Germany

Abstract

The noise radiated from distributed propellers could be a main problem for novel electrified aircraft concepts. This paper explores an aircraft propeller phase control technique for noise reduction over sensitive areas on the ground such as infrastructure near airports. The synchrophasing method proposed in this paper is based on an Extremum-Seeking Controller with improved gradient estimation through an extended Kalman filter. This method is evaluated via simulations for various configurations of the propulsion system, taking into account different number of propellers, number of blades, and other parameters. It was observed that the algorithm achieves better noise reduction when more degrees of freedom (number of propellers) are available for control. In some cases, an average reduction of almost 15 dB has been reached.

^{*}Research Fellow, Aeronautical Requirements and Control of Propulsion Systems

[†]Research Fellow, Aeronautical Requirements and Control of Propulsion Systems

[‡]Group Leader, Aeronautical Requirements and Control of Propulsion Systems

 $[\]S$ Department Head, Aeronautical Requirements and Control of Propulsion Systems, thomas.geyer@dlr.de

Nomenclature

 $\mathbf{0}$ = null vector

B = number of blades

 B_D = chord to diameter ra-

tio

BPF = Blade Passing Fre-

quency

 c_0 = speed of sound

EKF = Extended Kalman Fil-

ter

ESC = Extremum-Seeking

Controller

 J_{mB} = Bessel function of or-

der mB

 k_x, k_y = dimensionless chord-

wise wave numbers

m = harmonic number

n = number of slave pro-

pellers

 $M_x, M_r, M_T = \text{flight}, \text{ tip rotational}$

and section relative

Mach numbers

OSPL = Overall Sound Pres-

sure Level

p = number of observers

 $p_0 = 20\mu Pa$ = reference pressure

 \tilde{p}_i = root mean square

value of the sound pressure signal in the

i-th observer

 \mathbf{P}_i = covariance matrix of

variable i

 $P_m, P_{Vm}, P_{Lm}, P_{Dm} = \text{total} \text{ and sources}$

contributions refer to Fourier transform of the acoustic2pressure \mathbf{Q} = covariance matrix of process noise

 ${f R}$ = covariance matrix of measurement noise

r = total distance of the propeller considered to the microphone

 t_b = ratio of maximum thickness to chord

 V_{∞} = cruise speed

X = normalized chordwise coordinate

z = normalized radial coordinate of the blade

 θ = directivity angle

 μ_i = mean value of the normal distribution of variable i

 $\rho_0 = \text{ambient density}$ $\phi = \text{directivity gradient}$ $\varphi = \text{slave propellers angle}$

 $\Psi_V, \Psi_L, \Psi_D = \text{normalized source Fourier}$

transforms

 Ω_D = 2π Doppler frequency

 $\bar{\omega}_E$ = perturbation frequency of

the signals

 \mathcal{N} = Normal distribution

1 Introduction

Distributed electric propulsion systems constitute a promising concept for future electric aircraft. They feature multiple, small propellers driven by electric motors, usually distributed along the wingspan. The increased propulsive efficiency of this arrangement, along with the possibilities it opens regarding flight control and safety, make it an interesting approach, [13]. However, propellers are also known for their increased noise generation compared to other propulsion mechanisms, e.g. fans. The noise produced during flight is not only an annoying problem for passengers and crew, but also for populations near airports and airways. A substantial component of propeller noise is tonal at the Blade Passing Frequency (BPF) and its corresponding harmonics. The analysis of the noise produced is a complex undertaking that requires consideration of the interactions between propeller blades and the incoming flow.

Existing control techniques for propeller noise reduction focus primarily on minimizing the tonal noise, often by matching the speed of the propellers (propeller synchronization) or by matching the speed and additionally controlling the relative phase between the propellers (propeller synchrophasing). The first technique mitigates the beating noise that is generated as a consequence of the disturbed inflow, which introduces slight variations of the aerodynamic conditions on each blade, leading to a slight lack of uniformity in blade speed, as for example shown in [17]. The second technique enables a further noise reduction by finding a relative phase angle between the propellers that maximizes destructive interference between the sound signals of the different propellers.

Synchrophasing has a direct effect on the noise generation with negligible effects on the propulsion of the aircraft. This makes this method particularly suitable for noise attenuation. The concept has been shown to be effective for the reduction of cabin noise in military aircraft [3]. Different kinds of synchrophasing control methods are available and have been shown to work efficiently, including speed command correction and integrated speed/power command correction[11]. An experimental wind tunnel study on the noise reducing effect of synchrophasing was done by Turhan et al. [19], using two 2-bladed co-rotating propellers at a constant rotational speed of 5000 rpm. With no inflow (at static thrust conditions), they observed a tonal noise reduction of 8 dB at the first BPF and a decrease in overall sound pressure level (OSPL) of 2 dB. At inflow conditions an even larger noise reduction

was observed. In a recent study by Joseph et al. [12], an analytical expression was derived to calculate the tonal noise reduction for two or more identical propellers, both co-rotating (propellers spinning in the same direction), as well as counter-rotating (propellers spinning in opposite directions). They concluded that synchrophasing can be a highly effective noise reduction method for co-rotating propellers. Zarri et al. [21] examined the flow around three adjacent, co-rotating rotors using lattice Boltzmann simulations, highlighting aerodynamic interaction between propellers as the dominant source of the sound emitted by the distributed propeller system at the BPF. Their results also confirmed the potential of synchrophasing to reduce the noise through destructive acoustic interference. In a recent experimental study by Del Duchetto et al. [4], it was found that reductions of the overall sound pressure level of 3 dB to 6 dB are possible through synchrophasing, and that the inflow velocity does not affect that phase angle at which reductions occur at certain locations.

This paper studies the usage of an Extremum-Seeking Controller (ESC) to minimize the noise measured at sensible locations on the ground by adjusting the relative phase of the propellers during an overflight. First results of this method have been shown in [15], in which no relative motion between source and observer is considered. The present work considers, apart of the relative motion, different features of the propulsion system. The effects of changes in parameters such as the number of propellers on the wing, the interactions between co-rotating and counter-rotating propellers, or the number of blades.

Section 2 of the paper presents a far-field model of the plant. This model is fed with the parameters of the propellers and their relative phase angles, and it provides the absolute sound pressure values recorded on the designated observers. The ESC algorithm and the gradient estimation for noise reduction are presented in Section 3. Some discussions on the effect of the directivity of the noise are also presented here, which become crucial for the gradient estimation. Section 5 shows and discusses some simulation scenarios considered, while conclusions and further work are presented in Section 6.

2 Description of the Plant

Figure 1 shows a schematic representation of the noise detection problem being considered. An aircraft flying at a cruise speed of V_{∞} and a fixed altitude h. As it traverses its flight path, its propellers emit sound waves

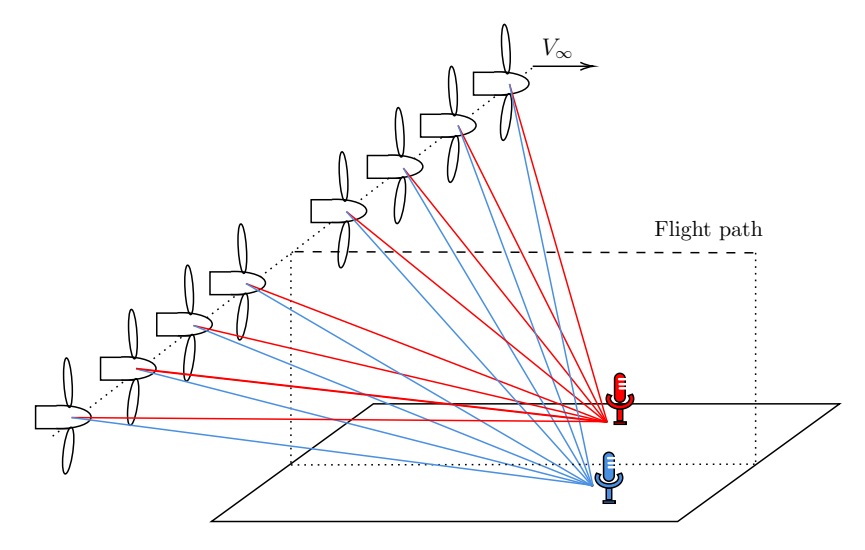


Figure 1: Schematic description of the problem addressed in the current paper.

that reach different observer locations on the ground. The noise perceived by these observers depends on the parameters of the system, such as the number of propellers, their rotational speed, their relative direction of rotation (coor counter-rotating), the number of blades on each propeller, the speed and altitude of the aircraft, and the location of the sensors. In addition, the relative phase between propellers directly affects the interference of the sound from both sources, and hence the noise level on the ground. This relative phase is the variable manipulated in this work.

To determine the sound pressure level during an overflight, a simulation tool was developed based on the Helicoidal Surface Theory framework introduced by Hanson [10, 8, 9]. This is a well established model which has been validated with acoustic tests performed in the NASA Lewis Wind Tunnel [6]. The developed tool considers three sources of noise per propeller: the volume displacement monopole P_V , the drag dipole P_D , and the lift dipole P_L . It does not take into account the quadrupole sources, as these sources are only important at high Mach numbers (their effect is comparable to that of the dipole sources when the Mach number is close to 1 [9]). In this study, subsonic speeds in the range $M_x < 0.4$ are considered, so the contribution of quadrupole sources is negligible.

The total sound pressure detected at any observer location can be ex-

pressed as a Fourier series as

$$p(t) = \sum_{m=-\infty}^{\infty} P_m \exp\left(-imB(\Omega_D t + \varphi)\right), \tag{1}$$

where the m^{th} harmonic coefficient,

$$P_m = P_{Vm} + P_{Dm} + P_{Lm}, (2)$$

is the sum of the contributions of the three aforementioned sources. The individual harmonic coefficients are found, as defined in [8], using

$$P_{Vm} = A \int \left(M_r^2 J_{mB} \left(z \frac{m B M_t \sin \theta}{1 - M_x \cos \theta} \right) \right) \left(k_x^2 t_b \Psi_V(k_x) \right) dz, \tag{3a}$$

$$P_{Dm} = A \int \left(M_r^2 J_{mB} \left(z \frac{m B M_t \sin \theta}{1 - M_x \cos \theta} \right) \right) \left(i k_x \frac{C_D}{2} \Psi_D(k_x) \right) dz, \quad (3b)$$

$$P_{Lm} = A \int \left(M_r^2 J_{mB} \left(z \frac{m B M_t \sin \theta}{1 - M_x \cos \theta} \right) \right) \left(-i k_y \frac{C_L}{2} \Psi_L(k_x) \right) dz, \quad (3c)$$

where Ψ_V , Ψ_D and Ψ_L are the functions for the volume displacement, drag sources, and lift sources in the frequency domain, respectively, and

$$A = -\frac{\rho_0 c_0^2 B \sin \theta \exp\left(i m B \left(\frac{\Omega_D r}{c_0} - \frac{\pi}{2}\right)\right)}{8\pi \frac{y}{D} (1 - M_x \cos \theta)},$$
 (4a)

$$k_x = \frac{2 m B B_D M_T}{M_r (1 - M_x \cos \theta)},$$
 (4b)

$$k_y = \frac{2 m B B_D M_T (M_r^2 \cos \theta - M_x)}{z M_r (1 - M_r \cos \theta)}.$$
 (4c)

Blade sweep and blade offsets can be considered in the Helicoidal Surface Theory as phase offsets. In this study, the simulation assumes ideal alignment of the blades and neither blade sweep nor offset, since the added complexity is out of the scope of this work.

The parameters of the plant used in the present study are initially based on the NASA SR-2 propeller (see, for example, [5]). The thickness ratio, diameter ratio, and blade section design lift coefficient are taken from [18]. However, a larger propeller diameter of 2.5 m is used. The chordwise distribution of thickness and lift coefficient for a NACA 16 profile are taken from

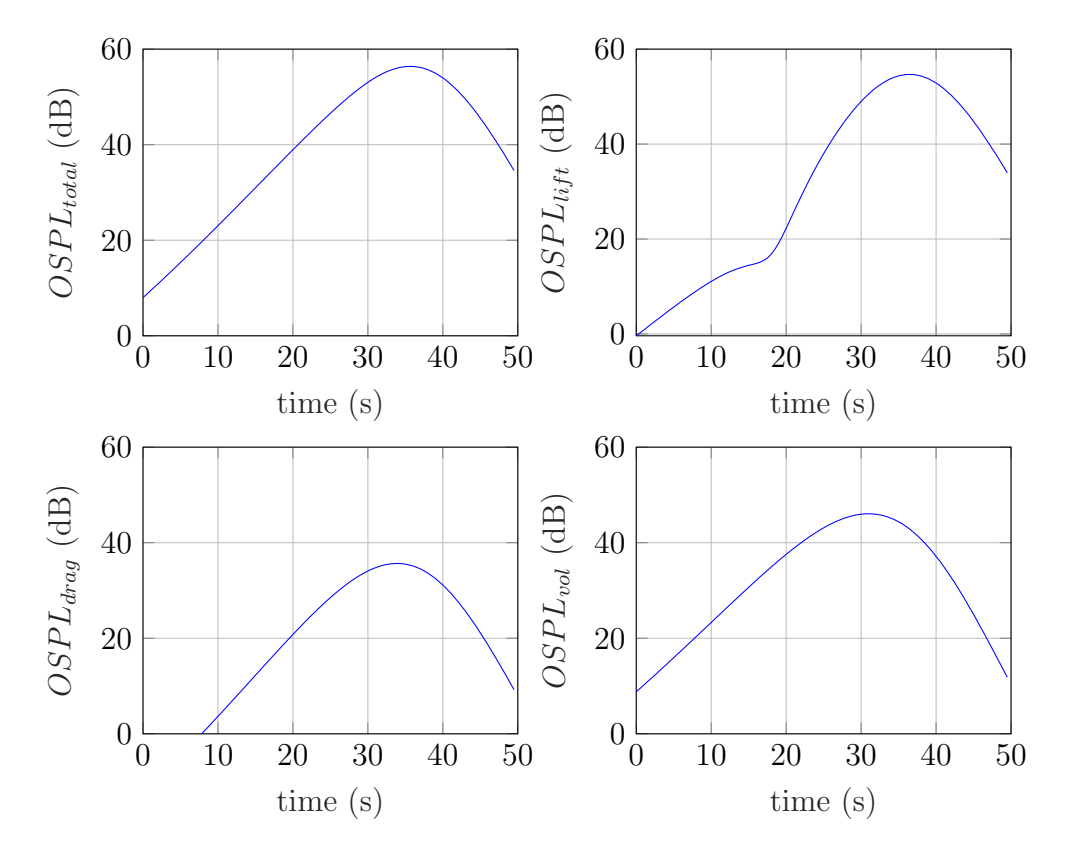


Figure 2: Decomposition of the contribution from the different source mechanisms to the total noise of the plant for an example overflight case.

[7], whereas the drag distribution has been assumed to be uniform. The number of blades of each propeller is considered as part of the study.

Figure 2 presents the results of a run of the simulation model. For the calculation, a sampling frequency of 8.192 kHz was chosen. The time signal was processed in blocks of 410 samples. Here, the noise generated by two propellers with eight blades each is shown in the form of the OSPL that contains all source mechanisms considered here, along the simulation time.

It can be observed that the dominant contributors to the noise in this case are the the volume monopole and the lift dipole, with the second one being more relevant as the aircraft approaches the observer and the first one taking over shortly before it overflies the observer. This is a result of the different directivities of the monopole and dipole noise sources in the direction of the flight. This confirms that the most important factor for an

overflight case is the directivity of the sound θ , defined as the angle between the flight path vector and the vector defined by the aircraft location and the observer location.

Another important factor is the direction of rotation of the propellers. Several studies have shown that synchrophasing works well for co-rotating propellers, but not for counter-rotating propellers. Thus, in the present study, the control algorithm is implemented on one or two groups of propellers, consisting of a Master and its Slaves, which are always co-rotating. Nevertheless, the full aircraft powertrain can still consist of two groups of propellers, which can have different directions of rotation.

3 Methodology

3.1 Control concept

To minimize the sound pressure level at the desired ground locations, an Extremum-Seeking Control (ESC) algorithm is proposed. This type of controller attempts to minimize the value of a given cost function by performing a gradient descent optimization in real time. The relatively simple control algorithm follows three steps:

- 1. The inputs to the plant are slightly disturbed.
- 2. The gradient of the cost function with respect to the disturbed input to the plant is estimated based on measurements.
- 3. The input value that provides the fastest gradient descent is calculated and applied applied to the plant.

The objective of this work is to minimize the OSPL measured at certain locations, so the cost function is formulated for a general case of n observers during a defined time window as

$$J = -10\log_{10} \left(\frac{\frac{1}{n} \sum_{i=1}^{n} \tilde{p}_i}{p_0} \right)^2 dB.$$
 (5)

This cost function directly depends on the sound pressure measured at each observer and can be tailored to accurately reflect the optimization objective.

Figure 3 describes the general structure of the ESC algorithm. The plant is fed with an input $\overline{u}_E \in \mathbb{R}^n$, which contains the relative phase angles

between the master and slave propellers. The output, $\bar{p}_s \in R^p$, is the total pressure registered by the observers and it is used to calculate scalar cost $J \in R$ using (5).

This cost and the initial disturbance \overline{u}_E are fed into the gradient estimation. This estimation is expected to provide a vector $g_E \in \mathbb{R}^n$ that indicates how much a change in one input affects the cost value. However, the actual effect might be masked by the fact that the sound pressure level caused by an aircraft approaching a target on the ground is always increasing. To cater for this, the directivity gradient $\phi(\theta)$ is also calculated in the plant and fed to the gradient estimation block. The signal $\phi(\theta)$ indicates how much the OSPL is expected to change due to a variation in the directivity angle θ , so that this can be separated from the actual contributions of the other inputs to obtain a correct g_E .

Each input of the plant is continuously disturbed by a perturbation function $\beta \sin(\overline{\omega}_E t)$. This is needed to cause variations in the inputs to the plant that make the estimation of a gradient always possible. The perturbation signals must have different frequencies for each input, such that $\omega_1 < \omega_2 < \cdots < \omega_n$. No frequency can be zero for any of the inputs and the period of these signals must be significantly larger than the largest time constant of the plant dynamics.

Integrating the gradient results in a biasing of the disturbed inputs to the plant as a step towards a local minimum of the cost function. The algorithm converges to a global extremum in case of a convex cost function. The factor $\alpha \in R$ is used to scale the integrator output, which is equivalent to controlling the step size of the gradient descent.

4 The Counter-rotating Propellers Case

When all propellers turn in the same direction, it is possible to define one propeller as a master and the rest as slaves. The Relative phase between them is easily defined. For two propellers rotating in opposite directions, it is not possible to define a relative phase angle. So, when counter-rotating propellers are considered, they will be separated in two groups, each one composed of one master propeller and its slaves, which are always co-rotating. Each group of propellers is considered to have its own independent controller.

The algorithm can be tuned using the following parameters:

• The coefficient α ,

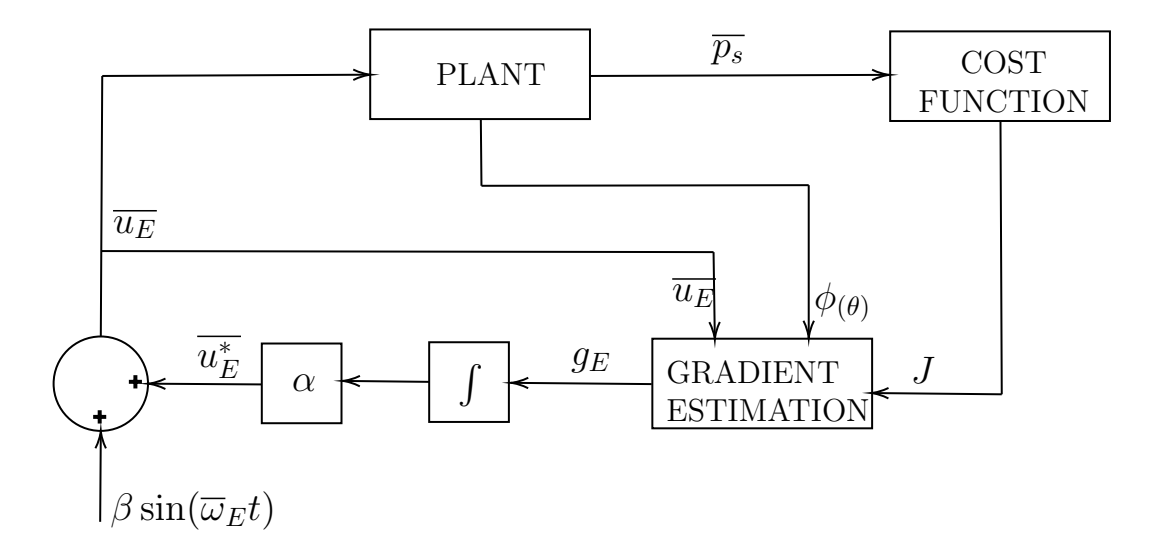


Figure 3: Block diagram of the Extremum-Seeking Controller method used.

- the amplitude of the perturbation signals, β ,
- the frequencies of the perturbation signals $\overline{\omega}_E$.
- the directivity gradient $\phi(\theta)$, which indicates when the noise is expected to increase or decrease regardless of the control.

An adequate excitation of the plant requires a trade-off. Large-amplitude signals lead to a fast convergence and noise immunity, but cause the plant to show significant oscillations at its output. Smaller amplitudes introduce less noticeable oscillations at the plant output, but may present a problem for an effective gradient estimation.

4.1 Gradient Estimation

Common methods for gradient estimation in ESC often use specific high-pass and low-pass filters [2, 16, 14]. This work uses an Extended Kalman Filter (EKF), based on work presented in [20], for the gradient estimation. This EKF is augmented with the estimation of effects of the directivity to improve the gradient estimation.

The gradient can be approximated as

$$\hat{g}_E(k) \approx \frac{\Delta y(k)}{\Delta u_E(k)} = \frac{(J(k) - J(k-1)) - \phi(\theta)}{u_E(k) - u_E(k-1)}.$$
 (6)

which considers as measurement vector the difference between the variation of the cost function value $\Delta J(k)$ and the directivity gradient $\phi(\theta)$. This parameter is modeled in the noise directivity study in section 4.2.

The initial condition for the gradient estimation is assumed to have a normal distribution

$$g_E(0) \sim \mathcal{N}_{g_E}(\mu_{g_E}(0), \mathbf{P}_{g_E}(0)).$$
 (7)

The rest of the stochastic model is then given by

$$g_E(k) = g_E(k-1), \tag{8}$$

$$\Delta y(k) = \Delta u_E(k) q_E(k). \tag{9}$$

For the prediction steps, the gradient state and the covariance matrix are estimated as

$$\hat{g}_E(k|k-1) = \hat{g}_E(k-1|k-1), \tag{10}$$

$$\mathbf{P}_{g_E}(k|k-1) = F\mathbf{P}_{g_E}(k-1|k-1)F^T + \mathbf{Q},$$
(11)

$$\mathbf{P}_{\Delta y}(k) = \Delta u_E(k) \mathbf{P}_{g_E}(k|k-1) \left(\Delta u_E(k)\right)^T + \mathbf{R}.$$
 (12)

The Kalman gain is computed as

$$\mathbf{K}(k) = \mathbf{P}_{q_E}(k|k-1) \left(\Delta u_E(k)\right)^T \left(\mathbf{P}_{\Delta y}(k)\right)^{-1}, \tag{13}$$

the predicted measurement is estimated as

$$\Delta \hat{y}(k) = \Delta u_E(k)\hat{q}_E(k|k-1),\tag{14}$$

and the corrections are carried out according to

$$\hat{g}_E(k|k) = \hat{g}_E(k|k-1) + \mathbf{K}(\Delta y - \Delta \hat{y}), \tag{15}$$

$$\mathbf{P}_{g_E}(k|k) = \mathbf{P}_{g_E}(k|k-1) - \mathbf{K}(k)\Delta u_E(k)\mathbf{P}_{g_E}(k|k-1).$$
 (16)

4.2 Noise Directivity

By lumping all terms not depending on θ into constants and considering that the integration is performed with respect to z, equations (3c) and (3a) can be reformulated such that they are proportional to a product of three independent functions of the directivity:

$$P_{Lm} \propto i A_1(\theta) J_{mB} (f(\theta)) \Psi_L(k_x(\theta)) \tag{17}$$

$$P_{Vm} \propto -A_2(\theta) J_{mB} \left(f(\theta) \right) \Psi_V(k_x(\theta)) \tag{18}$$

with

$$A_1(\theta) = \frac{\sin \theta}{\left(1 - M_x \cos \theta\right)^2} \left(M_r^2 \cos \theta - M_x\right) \tag{19}$$

$$A_{2}(\theta) = \frac{\sin \theta}{(1 - M_{x} \cos \theta)^{3}}$$

$$f(\theta) = k_{0} \frac{\sin \theta}{1 - M_{x} \cos \theta}$$
(20)

$$f(\theta) = k_0 \frac{\sin \theta}{1 - M_0 \cos \theta} \tag{21}$$

(22)

The influence of θ in Ψ_L is now considered. From [8], the expression for Ψ_L is

$$\Psi_L = \int_{-1/2}^{1/2} f_L(X) \exp(ik_x X) dX, \tag{23}$$

where f_L is a function describing the chordwise lift distribution and k_x is a so called chordwise wave number. Reference [7] shows the distribution of the effective pressure coefficient along the chord of a NACA 16 airfoil, from which the lift coefficient curve is obtained. A polynomial function has been used to represent this curve to simplify the further analytical integration. Figure 4 presents attempts with polynomials of different orders. A fourth-order polynomial is seen to provide a good fit without increasing the complexity too much.

With this polynomial, the integral becomes

$$\Psi_L = \int_{-1/2}^{1/2} (aw^4 + bw^3 + cw^2 + dw + e) \exp(ik_x w) dw, \qquad (24)$$

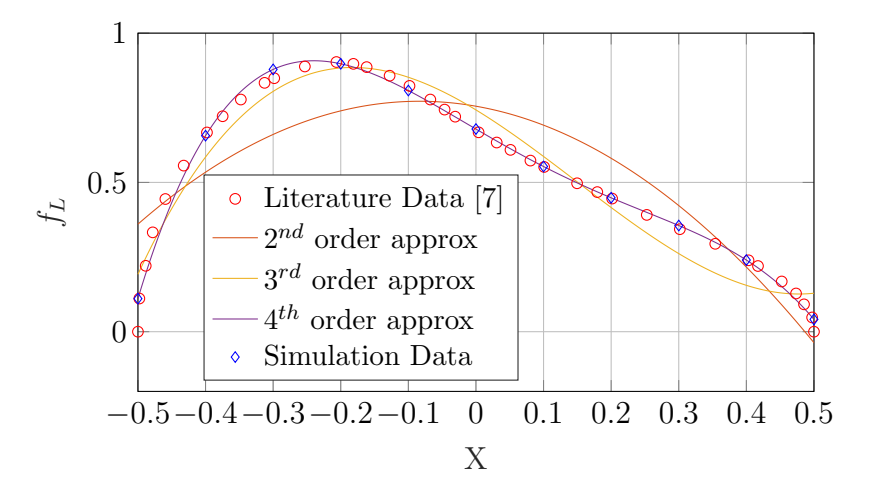


Figure 4: Comparison between different fits in 2^{nd} , 3^{rd} and 4^{th} order polynomials to the actual shape of the chordwise lift distribution.

and from here, an analytical expression for Ψ_L as a function of θ is obtained to be used in (17).

A similar procedure is followed for Ψ_V . In this case, the curve fitting of the thickness distribution is shown in Fig. 5.

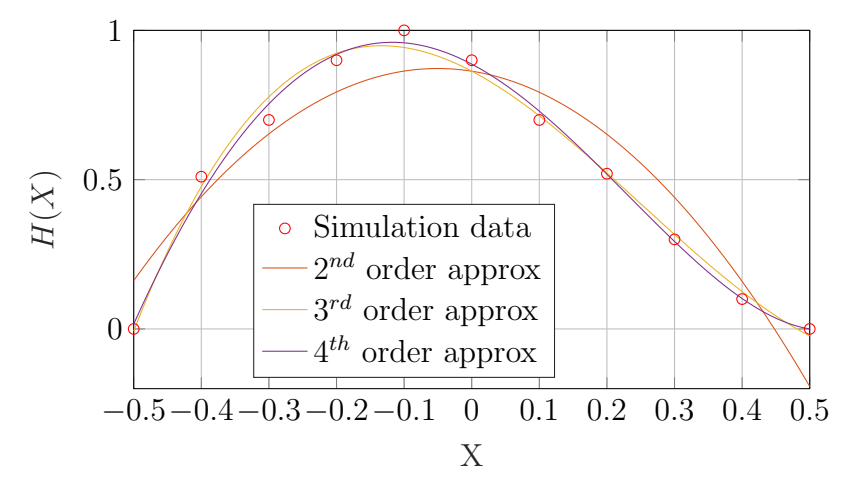
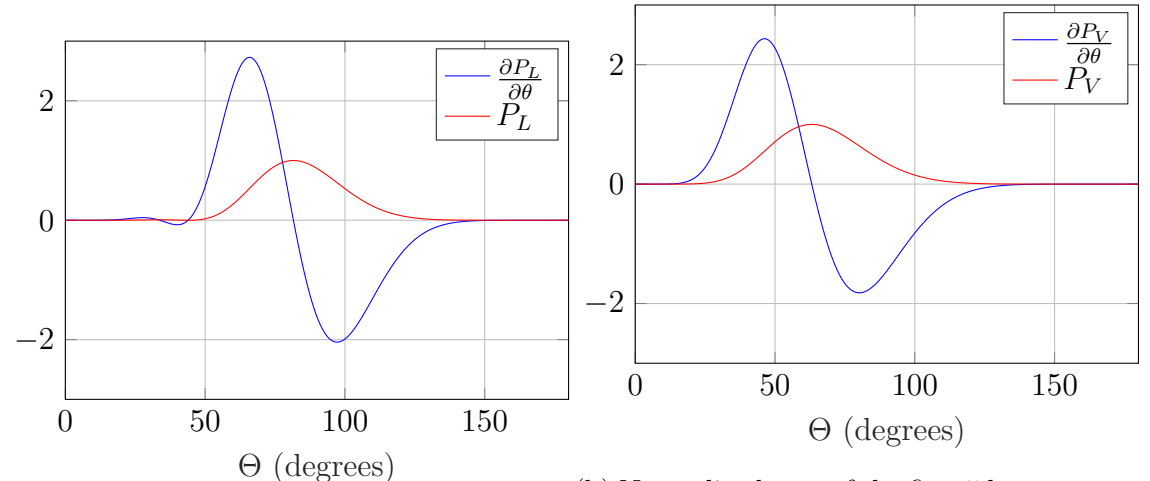


Figure 5: Comparison between different fits using 2^{nd} , 3^{rd} and 4^{th} order polynomials to the actual shape of the chordwise thickness distribution.



- (a) Normalized sum of the first 5 harmonics in the lift dipole directivity and its derivative.
- (b) Normalized sum of the first 5 harmonics in the volume displacement monopole directivity and its derivative

Figure 6: Normalized sum of the first 5 harmonics of the two dominant sources.

4.2.1 Directivity gradient

Obtaining the derivatives of (17) and (18) analytically is extremely demanding. These equations can nevertheless be used to estimate the gradient of the OSPL with respect to θ numerically to provide it to the control algorithm as already described. The results of this gradient estimation can be seen in Fig. 6. This figure shows the sum of the first five harmonics for each one of the sources, together with their gradient estimation.

The directivity of both sources can be appreciated in the polar coordinates as shown in Figure 7.

5 Results

Several simulations were performed to evaluate the effectiveness of the algorithm as a method of noise reduction. First MISO (Multiple Inputs, Single Output) cases are considered, in which a single observer is assumed to be present. Further results show how the the algorithm performs in MIMO

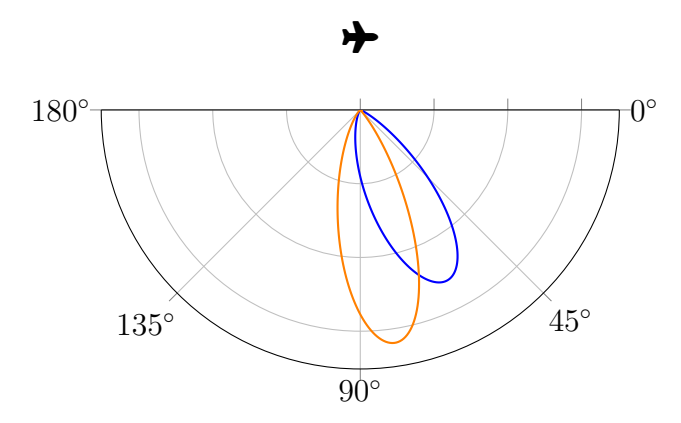


Figure 7: Polar representation of the directivity of lift dipole in orange and the volume displacement monopole in blue.

case (Multiple Inputs, Multiple Outputs) in which three uniformly spaced observers are considered.

The simulations are classified initially by the number of propellers on the aircraft, then by the relative direction of rotation and configuration, and then by the number of propeller blades used. Table 3 presents all cases considered for the MISO study with a specific label. The MIMO study focuses only on the cases 2A2, 2B2, 2C2.

The definition of co- and counter-rotating wing and mix configurations is clarified in Figure 8. For this configurations, as explained in Section 3, two independent controller run in parallel, one for each group of propellers.

All simulation cases ran with the same parameters in the controller, including the perturbation frequencies. These have been chosen as randomized between 0.4 an 0.8 $\frac{rad}{c}$.

Two metrics have been chosen to compare the results. Both are derived from the difference between the OSPL curve through the overflight simulation of the uncontrolled case and the controlled one, or Δ OSPL. First, the maximum attenuation is the maximum of the Δ OSPL. The other parameter is the average attenuation, which is the mean of Δ OSPL. The mean is only carried out from the moment in time where the effects of the control show up after the initial delay, so $t_{dom} = t_{sim} - t_{D,t=0}$. In addition, is important to mention that they must be positive if the control case obtains lower noise than the uncontrolled case, which is expected. The results are summarized in the tables 4 and 5.

Table 3: Presentation of the simulation cases and nomenclature explanation.

Number of Propellers	Configuration	Number of Blades	Label
Two	Co-rotating	6	1A1
1 WO	Co-rotating	8	1A2
	Co-rotating	6	2A1
	Co-rotating	8	2A2
Eight	Counter-wing	6	2B1
Eligit.	Counter-wing	8	2B2
	Counter-mix	6	2C1
	Counter-mix	8	2C2
	Co-rotating	6	3A1
	Co-rotating	8	3A2
Twelve	Count on win a	6	3B1
1 werve	Counter-wing 8		3B2
	Counter-mix	6	3C1
	Counter-IIIIX	8	3C2

5.1 MISO cases

First, a comparison between all the different cases regarding direction of rotation and configuration is performed, regarding the OSPL curves and the phase variations commanded by the control. The simulation cases with eight propellers and eight blades are performed: 2A2, 2B2, 2C2. The observer is located at $\frac{4}{5}$ of the trajectory in order to clearly present the data. Due to a cruise constant speed being assumed, the observer would be overpassed on $\frac{4}{5}$ of the total simulation time, which is 40 seconds. All of this can be observed in Figure 9 and Figure 10.

A maximum in the OSPL can be observed in the uncontrolled curve, around the 35 seconds mark. This was expected, matching with the directivity study carried out before. Moreover, all three configurations react in different ways. The counter-rotating configuration starts in the same way and it is only after a certain steps later that they diverge from each other. It is remarkable how the co-rotating case, in blue, converges when the decreasing noise segment is initiated. This can also be appreciated in the phases of figure 10, which this segment is initiated earlier, as the phases do not have the plant delay. Both counter-rotating cases achieve the convergence

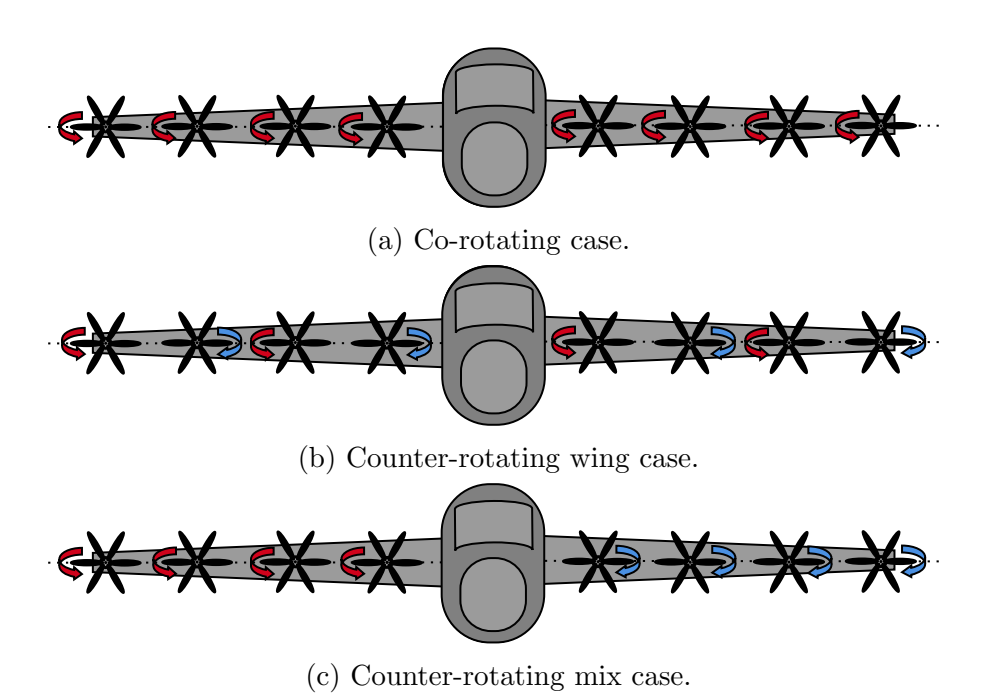


Figure 8: Rotational cases explored in the simulations for three different configurations of eight propellers aircraft.

later, in consequence, it seems that one group of propellers controlled by the ESC performs more consistent with 7 degrees of freedom than two groups of propellers operating by ESC with 3 degrees of freedom both. Although, the results of Table 5 indicates that the average reduction is greater for the counter-rotating cases. It should be noted that the labels of the phases represents the position of the slave propellers, beginning from the right wing of the aircraft. The main observation for Figure 10 is that for the counter-rotating configurations the phases react in pairs. In the convergence the phases of one group of propellers matches in symmetry with their respective number in the other group. On one hand, as the wing configuration disposes of control of the propellers in order for each wing, the phase 1 is matching with the 4, the 2 with the 5 and the 3 with the 6. On the other hand, the mix configuration has one propeller rotating to one side and the next one to the other, which is the reason why the propellers that match are: the 1 with the 2, the 3 with the 4 and the 5 with the 6. Regarding the results, for this case of eight propellers and eight blades, it appears to be that the counter-rotating configurations outperform the co-rotating one in both, maximum and average attenuation

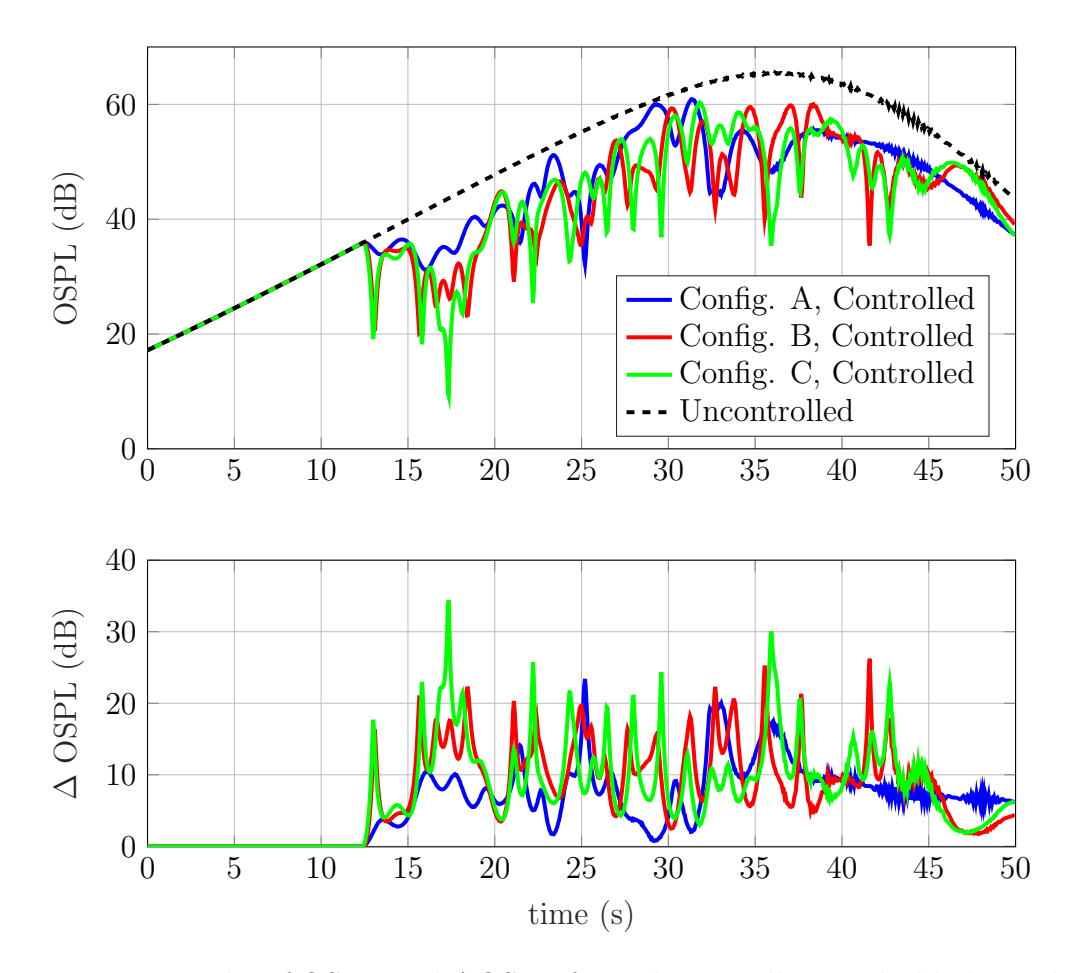
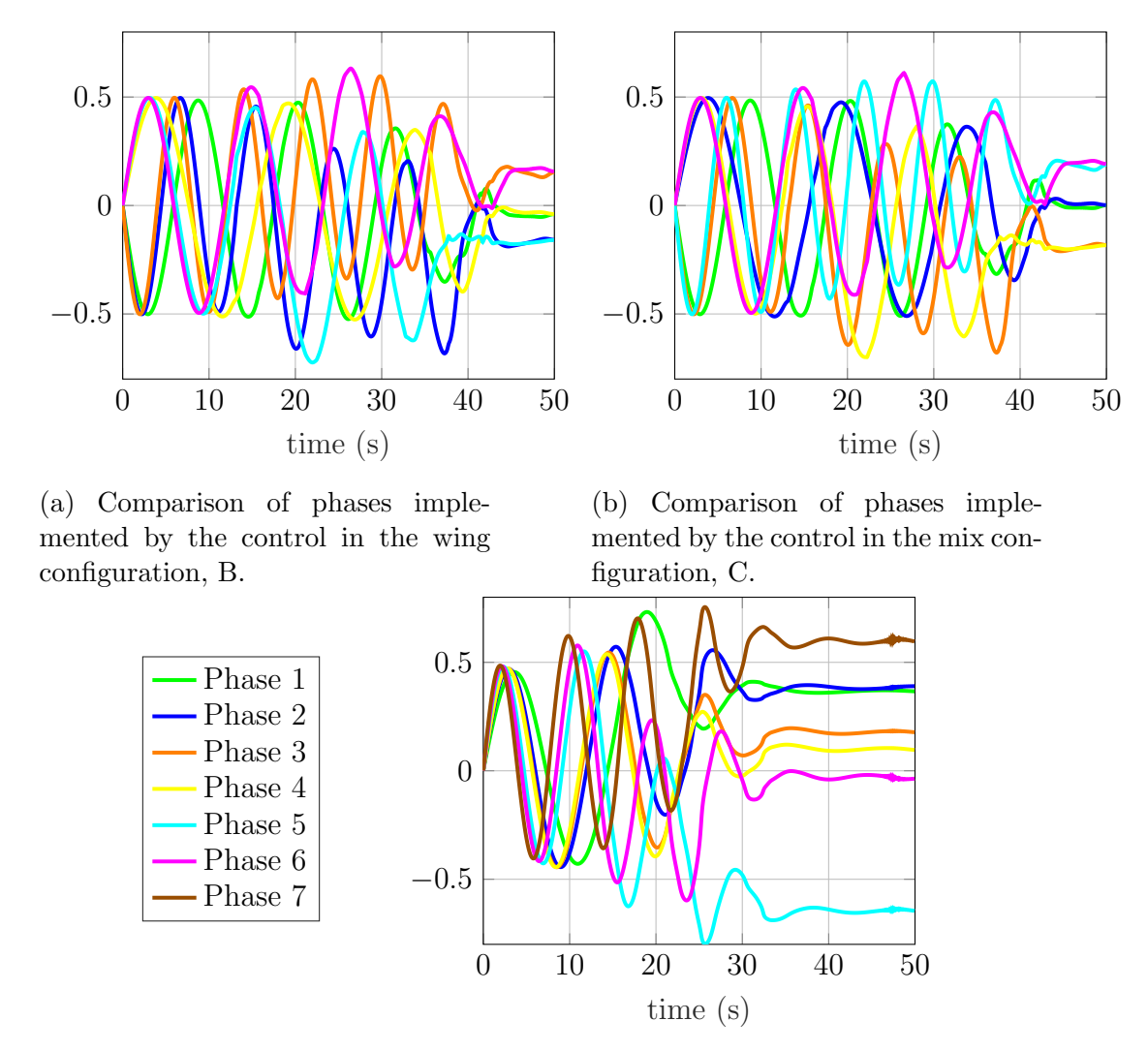


Figure 9: Results of OSPL and Δ OSPL for eight propellers, eight blades and the three different configurations.

of the Δ OSPL. Between both counter-rotating configurations, the mix one shows a slightly better performance.

Now a comparison between the difference of the number of blades is performed in the Figure 11, for two propellers, cases 1A1 and 1A2. As only one propeller can be controlled, the only configuration possible is the co-rotating configuration.

It can be appreciated that the case of the six blades produces more average noise without any control, around 6 dB of difference. In addition, the maximum peak of the six blades case is 60.9 dB, whereas the eight blades case reaches 56.5 dB. These results match with the literature, which agrees



(c) Comparison of phases implemented by the control in the co-rotating configuration, A.

Figure 10: Results for the simulations cases for eight propellers, eight blades and all three possible configurations.

that as less number of blades, more noise is produced [19, 1]. Regarding the controlled cases, the maximum attenuation achieved by the eight blades cases is 25.2 dB obtained just after the initial delay is elapsed. However, the six blades cases reaches the maximum attenuation later in the simulation

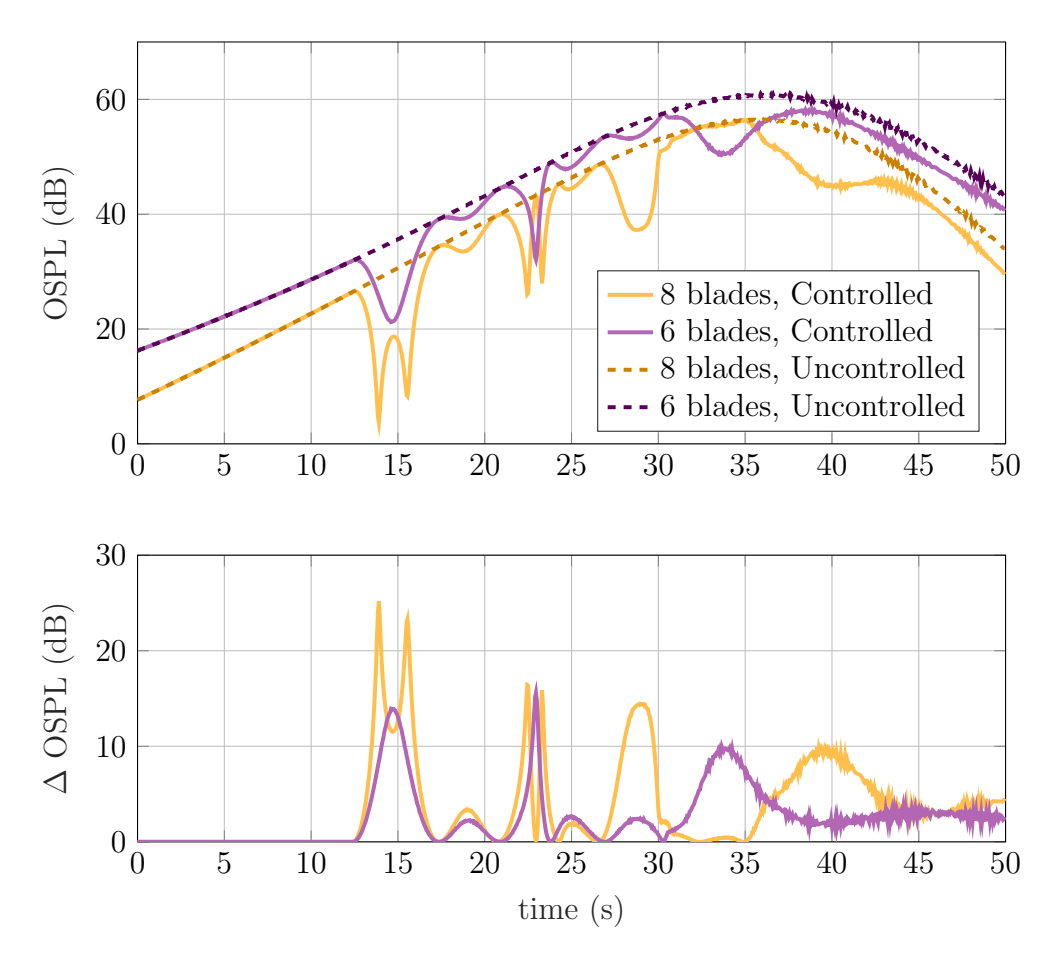


Figure 11: Results of the OSPL for two propellers and different number of blades.

with 15.6 dB. Moreover, the average attenuation of the Δ OSPL for the eight blade cases is greater than for the six blades case, as it can be appreciated in the tables 4 and 5. As a result, the cases of six blades produces naturally more noise and the attenuation achieved by the control algorithm is lower than for the eight blade case.

Returning to the eight propeller's cases, the Figure 12 shows a quick comparison in $\Delta OSPL$ for all the configurations with six blades of cases 2A1, 2B1, 2C1. Figure 12 is closely related to the figure 9, however some differences can be appreciated. First the counter-rotating cases presents almost the same average reduction, their performance is superior to the co-rotating configuration

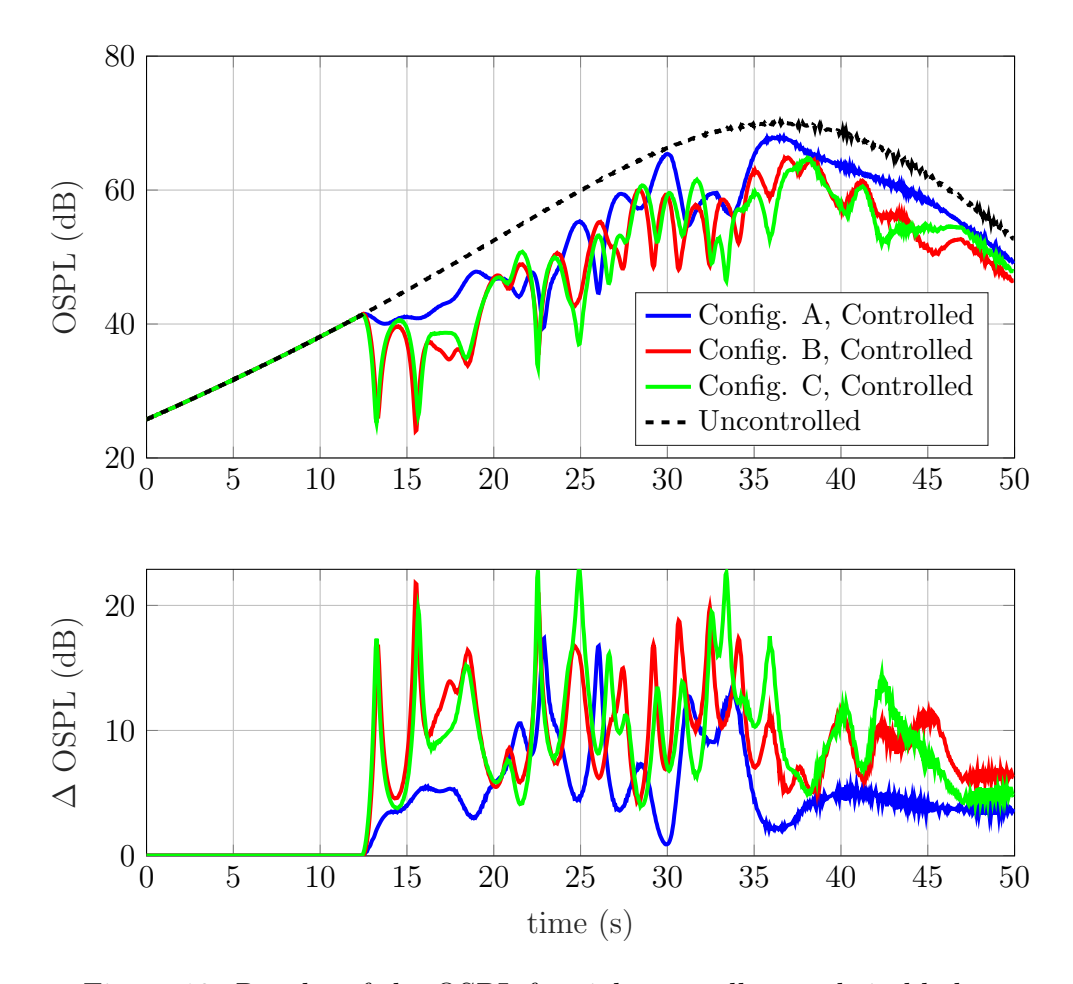


Figure 12: Results of the OSPL for eight propellers and six blades.

by 4 dB. Moreover, the maximum attenuation achieved by the co-rotating case is around also 4 dB lower than the wing counter-rotating case, which has a barely lower maximum than the mix counter-rotating case. As consequence, for the set of simulations of eight propellers, the counter-rotating cases perform better than the co-rotating case.

Advancing with the twelve propeller cases, on one hand, the Figure 13 shows OSPL values for all the configuration with six blades and on the other hand, the Figure 14 shows the respective results for eight blades.

Comparing the results from the eight with the twelve propellers, there are some substantial differences. The difference is notorious in the six blades study case, Figure 13. There, the co-rotating case improves, nearly matching

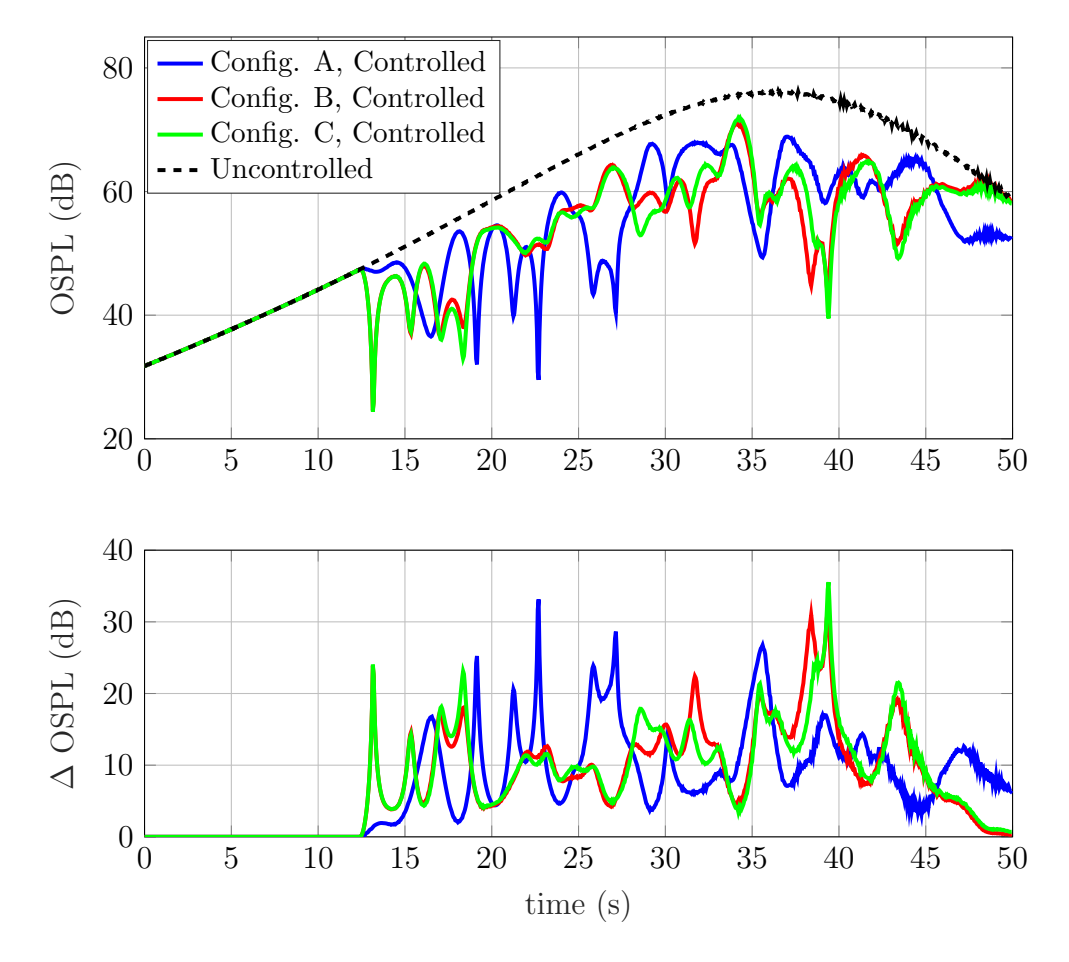


Figure 13: Results of the OSPL and Δ OSPL for twelve propellers, six blades and all three possible configurations.

the performance of both counter-rotating cases. However, the average attenuation is slightly lower than both counter-rotating configurations, which share the same value. The mix configuration shows better behavior than the wing one for the maximum attenuation. For the eight blades study, Figure 14, the co-rotating configuration obtains more than 3 dB greater average attenuation than the best performance of counter-rotating configurations, with almost a total of 15 dB compared to the uncontrolled case. The reduction is mainly effective and consistent after the observer has been overpassed. The maximum attenuation of the co-rotating case is not that good, it is slightly better than the wing counter-rotating configuration and 5 dB worse that the

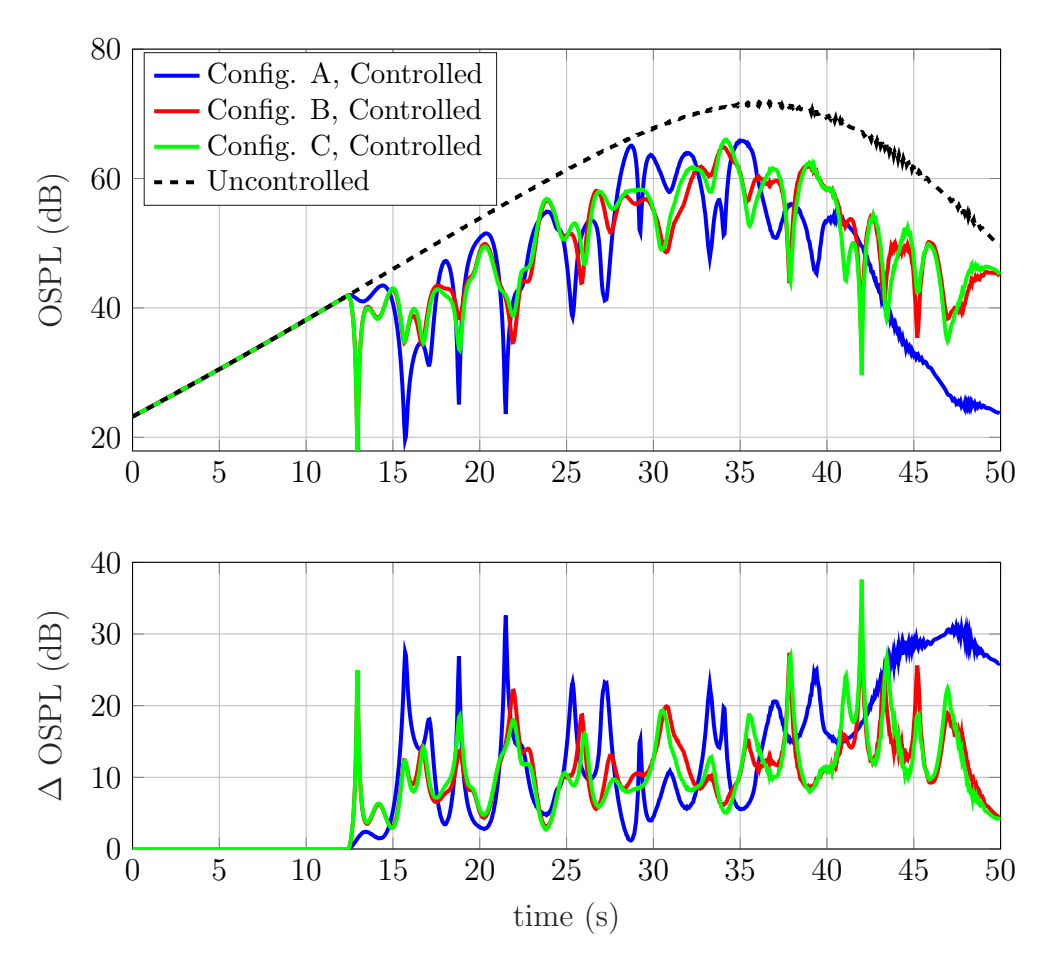


Figure 14: Results of the OSPL and Δ OSPL for twelve propellers, eight blades and all three possible configurations.

mix configuration.

Some last notes about these tables are that the number of propellers is proportional to the noise measure. Moreover, the strategy of one group of propellers controlled by ESC for a co-rotating configurations performs worse as less degrees of freedom the algorithm have, or propellers for controlling. The strategy of two group of propellers, or counter-rotating configurations, proves advantageous over the single-group or co-rotating configuration one, especially when the control, systems have fewer degrees of freedom. However, as much as degrees of freedom are taking into account the co-rotating configuration outperforms both counter-rotating configurations. Furthermore,

Table 4: Results maximum peak noise and average noise attenuation regarding the uncontrolled case for six blades propellers.

N_{prop}	Configuration	Maximum attenuation (dB)	Average attenuation (dB)	
2	A	15.6	3.3	
	A	17.4	5.6	
8	В	21.8	9.6	
	С	22.9	9.5	
	A	33.1	10.1	
12	В	31.7	10.5	
	С	35.5	10.5	

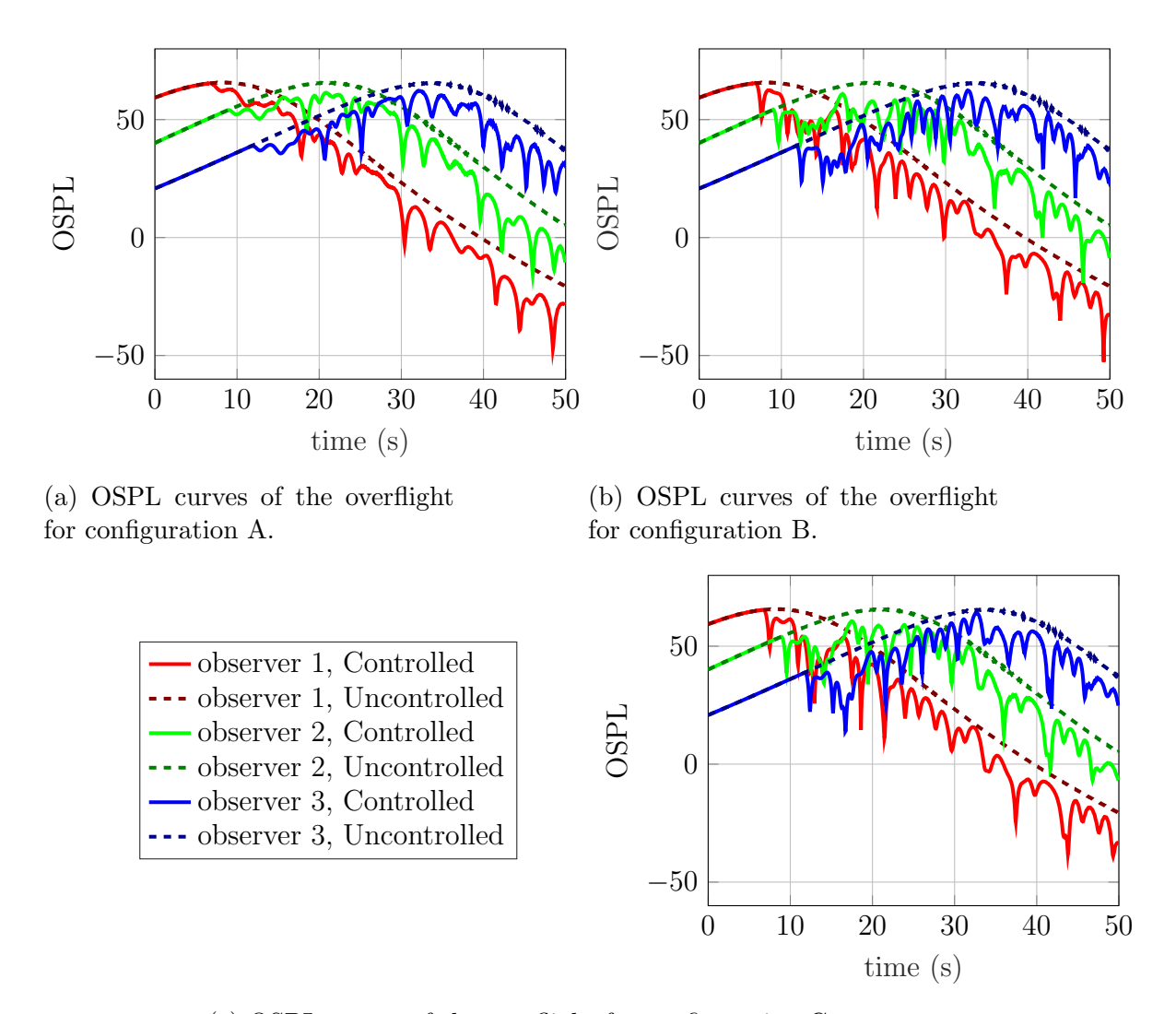
Table 5: Results maximum peak noise and average noise attenuation regarding the uncontrolled case for eight blades propellers.

N_{prop}	Configuration	Maximum attenuation (dB)	Average attenuation (dB)	
2	A	25.2	4.8	
	A	23.4	8.0	
8	В	26.2	9.8	
	С	34.4	9.9	
	A	32.6	14.5	
12	В	31.6	11.1	
	С	37.6	11.0	

the difference between both counter-rotating configuration is really small. Nevertheless, the mix configuration has shown slightly better behavior in average attenuation and the wing one in maximum attenuation. In addition, the best performance of the algorithm regarding the average attenuation is with twelve propellers, co-rotating configuration and eight blades, with almost 15 dB. While the maximum attenuation has been performed by the counter-rotating mix configuration with twelve propellers, with eight blades too.

5.1.1 MIMO cases

For the last results three MIMO case are performed, where three observers are on the ground. For that, the directivity gradient must be averaged in the next way $\phi = \frac{\phi(\theta_1) + \phi(\theta_2) + \phi(\theta_3)}{3}$. Here, there are three different angles, one for



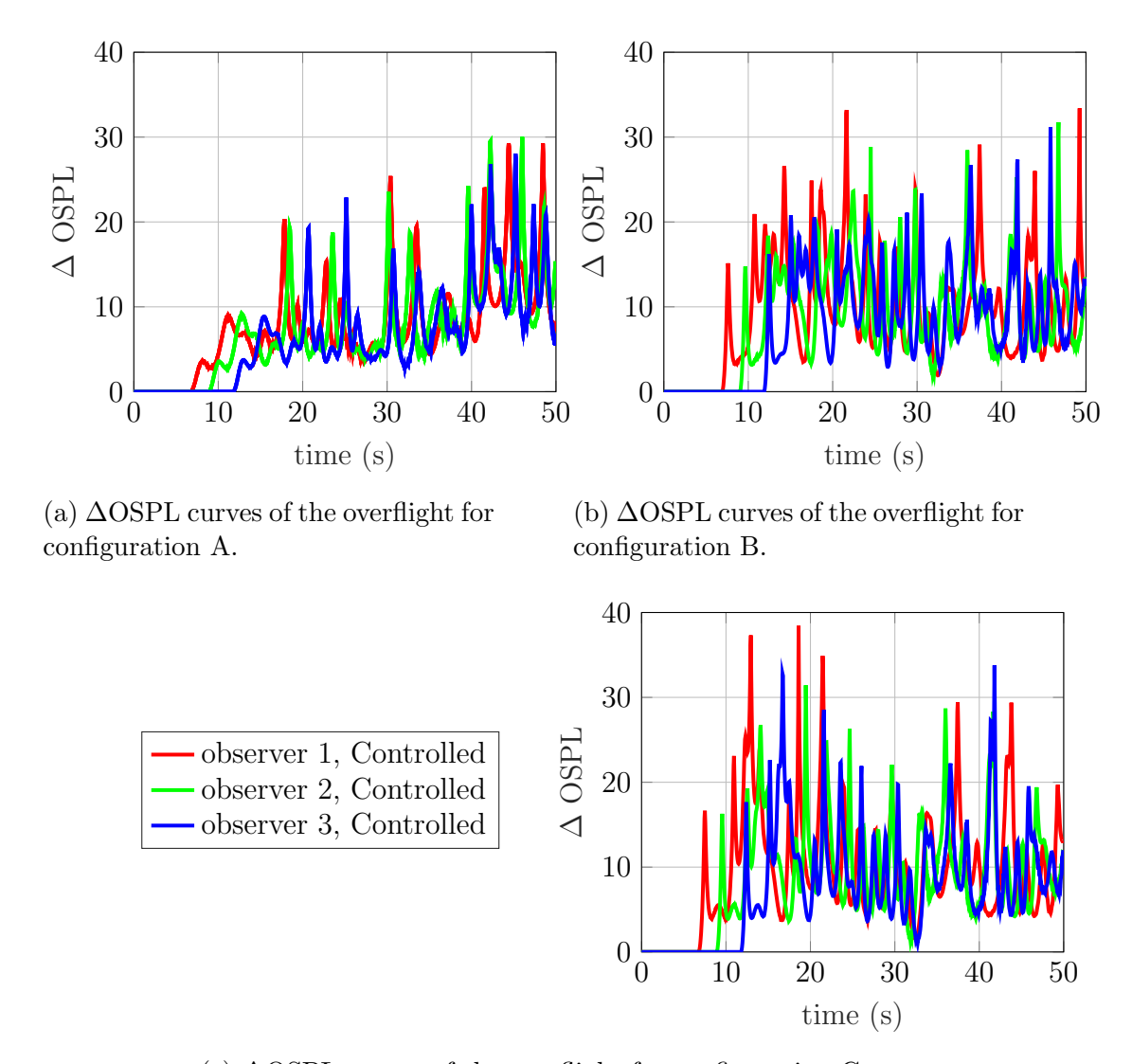
(c) OSPL curves of the overflight for configuration C.

Figure 15: Results of the OSPL in a MIMO case for eight propellers and eight blades with the observers in a distance of $\frac{1}{4}$, $\frac{1}{2}$ and $\frac{3}{4}$ of the total distance of the overflight.

each observer.

These MIMO cases, in Figure 15, are going to explore all the configurations of eight propellers and eight blades, cases 2A2, 2B2, 2C2.

Looking to Figure 15, Figure 16 and the table 6 several findings can



(c) \triangle OSPL curves of the overflight for configuration C.

Figure 16: Results of the Δ OSPL in a MIMO case for eight propellers and eight blades with the observers in a distance of $\frac{1}{4}$, $\frac{1}{2}$ and $\frac{3}{4}$ of the total distance of the overflight.

be derived from the data. First the distance of each observer impacts on the algorithm performance in a MIMO case due to the delay. As it can be observed in the last figures, the effects of the algorithm are not visible at

Table 6: Results maximum peak noise and average noise attenuation regarding the uncontrolled case for eight blades, eight propellers and all three configurations possible.

	Configuration	Maximum attenuation (dB)		Average attenuation (dB)			
\	Observer \rightarrow	1	2	3	1	2	3
	A	29.3	30.0	28.0	8.7	8.8	8.4
	В	33.4	31.7	31.2	10.5	10.1	10.3
	С	38.4	31.4	33.8	10.7	10.1	9.9

the same time. First, it is appreciated in the observer one located at $\frac{1}{4}$ of the total distance, then to the second and the third located at $\frac{1}{2}$ and $\frac{3}{4}$ of the total distance. This different delay has a huge impact on the results. It seems that the closer the observer is, the greater the maximum and average attenuation will be. Moreover, Figure 16 shows that the Δ OSPL increases mainly in the segment of the simulation where more uniform is the directivity gradient in all of the observers. Regarding the main results, the same trend as the corresponding MISO cases can clearly be observed, where the counterrotating cases, B and C outperforms the co-rotating case, A.

In these cases the phases does not converge due to the more chaotic behavior resulting from having different points where the noise must be minimized, despite that they follow a visible trend in their trajectory under the uncontrolled curves. Nevertheless, this predisposition makes the algorithm to obtain a good attenuation, greater as sooner the observer is overpassed. The data is collected in the table 6. Here it is important to note that the algorithm still works after the OSPL goes under 0 dB in some observers. This is because the function minimizes the overall sound pressure level considering the contributions from all observers.

The data clearly shows that in the line of the MISO results for eight propellers, the counter-rotating continue performing better than the co-rotating configuration. However, both wing and mix configurations do not exhibit a clear overall performance advantage. On one hand, for the average attenuation, the mix configuration performs better for the first observer, on the other hand the wing configuration shows advantage in the third observer results. The mix configuration still exhibits the best performance in maximum attenuation.

6 Conclusion

A parametric study of propeller synchrophasing for noise reduction using an Extremum Seeking control algorithm with improved gradient estimation is presented. The main difference with previous studies was the exploration of dynamic cases, with relative motion between source and observers. This required an introduction of an extra term into the gradient estimation technique part of the whole ESC algorithm scheme.

The effect of several parameters has been explored, like the number of propellers and the number of blades of each propeller. From the control point of view, the configuration of the noise reduction control strategy was analyzed. Two main configurations have been taking into account, the corotating one, based in one master propeller at the tip of the right wing of the aircraft and the rest of the slave propellers. While the counter-rotating configuration is based in one group of propellers rotating in clockwise direction with the master propeller at the tip of one wing and another group rotating in the opposite direction with its master propeller at the tip of the other wing. The main goal has been achieved with a great reduction both from the average OSPL and the maximum attenuation of OSPL along the whole simulation. The control performance improves with the availability of additional degrees of freedom or slave propellers, obtaining the greatest attenuation for the twelve propellers case.

In first place the results are consistent with the expectations regarding the increase of natural noise with the decrease of the number of blades of each propeller and with the increase of propellers.

This study also shows that there is no global best configuration for noise reduction. Depending of each case one configuration is more suitable than others. The idea of using two groups of propellers for representing the counter-rotating configuration has exhibited a great behavior mainly for cases with a moderate number of propellers and a notable behavior for cases with more number of propellers. However, it is concerning the fluctuation that these configurations implies. If a choice has to be made in terms of overall performance for the counter-rotating configuration, the mix configuration would be selected over the wing one. The co-rotating configuration has shown a worse performance for a moderate number of propellers cases and it has only being dominant for the case of twelve propellers and eight blades. Nevertheless, this attempt has been the best of all the study and the control presents more controlled oscillations than the other configurations. As a re-

sult, the co-rotating configuration can not perform optimally in every case, albeit offering greater stability. Hence, from a control point of view, this option is really suitable. Furthermore, to have one group of propellers scheme is simpler than two as the counter-rotating configurations. Gathering all of that, the most suitable option is to chose the co-rotating configuration for a noise reduction via synchrophasing in a overflight of an aircraft. These results open a door for further discussion about other types of active control techniques as well as variations of control schemes that can help to reduce the noise in distributed propulsion aircraft.

It is important to note that in this study the reflection with the ground effect has not being considered due to the assumption of the microphones on the ground.

Future work includes analyzing the effect of synchrophasing on cabin noise.

7 Acknowledgments

The project was carried out in the framework of the DLR-internal program H2EAT – Vergleich hoch-integrierter brennstoffzellenbasierter elektrifizierter Antriebstopologien.

References

- [1] Kabilan Baskaran, Nur Syafiqah Jamaluddin, Alper Celik, Djamel Rezgui, and Mahdi Azarpeyvand. Effects of number of blades on propeller noise. *Journal of Sound and Vibration*, 572:118176, 2024.
- [2] Ralf Becker, Rudibert King, Ralf Petz, and Wolfgang Nitsche. Adaptive closed-loop separation control on a high-lift configuration using extremum seeking. *AIAA Journal*, 45(6):1382–1392, 2007.
- [3] David Blunt and Brian Rebbechi. Propeller synchrophase angle optimisation study. In 13th AIAA/CEAS Aeroacoustics Conference (28th AIAA Aeroacoustics Conference), page 3584, 2007.
- [4] Fabio Del Duchetto, Tiziano Pagliaroli, Paolo Candeloro, Karl-Stéphane Rossignol, and Jianping Yin. Aeroacoustic study of synchronized rotors. *Aerospace*, 12(2):162, 2025.

- [5] James H Dittmar. Cruise noise of the SR-2 propeller model in a wind tunnel. Technical Memorandum TM 101480, 1989.
- [6] James H Dittmar, Bernard J Blaha, and Robert J Jeracki. Tone noise of three supersonic helical tip speed propellers in a wind tunnel at 0.8 mach number. Technical report, NASA Lewis Research Center, 1978.
- [7] Federal Aviation Administration. Aeronautical circular no. 2 (anc-2). Technical report, Federal Aviation Administration (FAA), 1942.
- [8] Donald B Hanson. Helicoidal surface theory for harmonic noise of propellers in the far field. *AIAA journal*, 18(10):1213–1220, 1980.
- [9] Donald B Hanson. Influence of propeller design parameters on farfield harmonic noise in forward flight. AIAA Journal, 18(11):1313–1319, 1980.
- [10] Donald B Hanson and Martin R Fink. The importance of quadrupole sources in prediction of transonic tip speed propeller noise. *Journal of Sound and Vibration*, 62(1):19–38, 1979.
- [11] Xianghua Huang, Yangyang Wang, and Long Sheng. Synchrophasing control in a multi-propeller driven aircraft. In 2015 American Control Conference (ACC), pages 1836–1841. IEEE, 2015.
- [12] Phillip Joseph, Chaitanya Paruchuri, Stephen Elliott, Mansi Bhardwaj, and Tze Pei Chong. Propeller tonal noise reductions through synchrophasing: Mechanisms and performance. *Journal of Sound and Vibration*, 610:119110, 2025.
- [13] Dennis Keller. Towards higher aerodynamic efficiency of propeller-driven aircraft with distributed propulsion. *CEAS Aeronautical Journal*, 12(4):777–791, 2021.
- [14] Miroslav Krstić. Performance improvement and limitations in extremum seeking control. Systems & Control Letters, 39(5):313–326, 2000.
- [15] Andrés Lopez Pulzovan, Gaurav Bokil, and Thomas F. Geyer. An application of an extremum-seeking algorithm with improved gradient estimation for propeller noise control. In 30th International Congress on Sound and Vibration, 2024.

- [16] R Maury, M Koenig, L Cattafesta, P Jordan, and J Delville. Extremum-seeking control of jet noise. *International Journal of Aeroacoustics*, 11(3-4):459–473, 2012.
- [17] F. Pla, G. Goodman, R. Ranaudo, and R Silcox. Cabin noise cancellation using active rpm control ov 10a flight test results. 15th AIAA/Aeroacoustics Conference, 1993.
- [18] George L Stefko and Robert J Jeracki. Wind-tunnel results of advanced high-speed propellers at takeoff, climb, and landing mach numbers. Technical report, 1985.
- [19] Burak Turhan, Hasan Kamliya Jawahar, Abhishek Gautam, Shahjahan Syed, Gaurang Vakil, Djamel Rezgui, and Mahdi Azarpeyvand. Acoustic characteristics of phase-synchronized adjacent propellers. *The Journal of the Acoustical Society of America*, 155(5):3242–3253, 2024.
- [20] S. Wolff. Entwicklung von Fehlererkennungs-, Zustandsschätzungs-, Regelungs- und ganzzahligen Optimalsteuerungsmethoden für pulsierende, detonative Brennkammern anhand eines akustischen Ersatzsystems. Ph.d. thesis, TU Berlin, Berlin, Germany, 2019.
- [21] A Zarri, F de Prenter, F Avallone, Daniele Ragni, and Damiano Casalino. Effects of phase synchronization on the tonal sound directivity of distributed propellers. *The Journal of the Acoustical Society of America*, 157(5):3267–3281, 2025.